The Astrophysical Journal, 932:100 (8pp), 2022 June 20 https://doi.org/10.3847/1538-4357/ac6b9f

Using the Sun to Measure the Primary Beam Response of the Canadian Hydrogen Intensity Mapping Experiment

The CHIME Collaboration,
Mandana Amiri[1], Kevin Bandura[2], Anja Boskovic[1], Jean-François Cliche[3], Meiling Deng[1,4,5], Matt Dobbs[3], Mateus Fandino[1,6], Simon Foreman[4,5], Mark Halpern[1], Alex S. Hill[4,7], Gary Hinshaw[1], Carolin Höfer[1], Joseph Kania[8], T. L. Landecker[4], Joshua MacEachern[1], Kiyoshi Masui[9,10], Juan Mena-Parra[9], Laura Newburgh[11], Anna Ordog[4,7], Tristan Pinsonneault-Marotte[1], Ava Polzin[12], Alex Reda[11], J. Richard Shaw[1], Seth R. Siegel[3], Saurabh Singh[3,13], Keith Vanderlinde[14,15], Haochen Wang[9,10], James S. Willis[15], and Dallas Wulf[3]
[1] Department of Physics and Astronomy, University of British Columbia, Vancouver, BC, Canada
[2] Department of Computer Science and Electrical Engineering, West Virginia University, Morgantown WV, USA
[3] Department of Physics, McGill University, Montreal, QC, Canada; dallas.wulf@mail.mcgill.ca
[4] Dominion Radio Astrophysical Observatory, Herzberg Astronomy & Astrophysics Research Centre, National Research Council Canada, Penticton, BC, Canada
[5] Perimeter Institute for Theoretical Physics, Waterloo, ON, Canada
[6] Department of Physical Sciences, Thompson Rivers University, Kamloops, BC, Canada
[7] Department of Computer Science, Math, Physics, and Statistics, University of British Columbia-Okanagan, Kelowna, BC, Canada
[8] Department of Physics and Astronomy, West Virginia University, Morgantown, WV, USA
[9] MIT Kavli Institute for Astrophysics and Space Research, Massachusetts Institute of Technology, Cambridge, MA, USA
[10] Department of Physics, Massachusetts Institute of Technology, Cambridge, MA, USA
[11] Department of Physics, Yale University, New Haven, CT, USA
[12] Department of Astronomy, Yale University, New Haven, CT, USA
[13] Raman Research Institute, Sadashivanagar, Bengaluru, India
[14] David A. Dunlap Department of Astronomy & Astrophysics, University of Toronto, Toronto, ON, Canada
[15] Dunlap Institute for Astronomy and Astrophysics, University of Toronto, Toronto, ON, Canada
Received 2022 January 27; revised 2022 April 25; accepted 2022 April 27; published 2022 June 20

Abstract

We present a beam pattern measurement of the Canadian Hydrogen Intensity Mapping Experiment (CHIME) made using the Sun as a calibration source. As CHIME is a pure drift-scan instrument, we rely on the seasonal north–south motion of the Sun to probe the beam at different elevations. This semiannual range in elevation, combined with the radio brightness of the Sun, enables a beam measurement that spans ∼7200 square degrees on the sky without the need to move the telescope. We take advantage of observations made near solar minimum to minimize the impact of solar variability, which is observed to be <10% in intensity over the observation period. The resulting data set is highly complementary to other CHIME beam measurements—both in terms of angular coverage and systematics—and plays an important role in the ongoing program to characterize the CHIME primary beam.

Unified Astronomy Thesaurus concepts: Radio telescopes (1360); Interferometers (805); Calibration (2179); Quiet sun (1322)

1. Introduction

The Canadian Hydrogen Intensity Mapping Experiment (CHIME) is a drift-scan radio interferometer array operating between 400 and 800 MHz. It consists of four parabolic cylindrical reflectors. Each reflector is 20 m in diameter, 100 m in length, oriented north–south, and is instrumented with 256 dual-polarization feeds that are sensitive to linear polarization in the north–south and east–west directions (1024 total feeds). This configuration provides a large instantaneous field of view, with the main lobe spanning ∼300 square degrees along the local meridian. CHIME is thus optimized for high mapping speed, making it a powerful instrument for 21 cm cosmology, transient detection, and source monitoring. For a more detailed description of CHIME, we refer the reader to CHIME Collaboration et al. (2022a) and references therein.

One of the challenges of working with CHIME is characterizing the large primary beam without the ability to steer the telescope. Due to the fixed pointing of the telescope, astrophysical radio sources that are typically used for beam measurements only transit the beam at a single declination. Thus, each source probes only a small fraction of the total beam solid angle. Moreover, few of these sources are bright enough to rise above the confusion level and be seen in the far side lobes. These challenges are shared by all drift-scan instruments with limited pointing capability, such as the Molonglo Observatory Synthesis Telescope (MOST; Bailes et al. 2017), the Deep Synoptic Array (DSA-110; Kocz et al. 2019), the Canadian Hydrogen Observatory and Radio transient Detector (CHORD; Vanderlinde et al. 2019), the Tianlai Project (Phan & Collaboration 2020), and the Hydrogen Intensity and Real-time Analysis eXperiment (HIRAX; Crichton et al. 2022). While some of these instruments are exploring the use of drones to overcome these challenges (e.g., Zhang et al. 2021), they are not feasible for CHIME, which has a far-field distance greater than one kilometer.

These considerations motivated us to use the Sun as a calibration source for measuring the primary beam response of CHIME. The Sun has been used for beam-mapping purposes before (e.g., Pauliny-Toth & Shakeshaft 1962; Murphy 1993; Higgs & Tapping 2000; Chang et al. 2015). However, these measurements were made with fully steerable dishes, capable of measuring the full beam in a single observation by employing a raster scan strategy. In contrast, the measurement reported here relies on the seasonal motion of the Sun and combines observations spanning one year. Between the winter and summer solstices, the decl. of the Sun moves between $-23.5°$ and $+23.5°$, enabling a quasi-continuous measurement of the beam over this range. Moreover, the radio brightness of the Sun exceeds 200 kJy in our band, enabling a high signal-to-noise measurement of the beam into the far side lobes. These combined properties enable the Sun to probe the beam over ∼7200 square degrees on the sky without the need to move the telescope.

In what follows, we describe a measurement of the CHIME primary beam made using the Sun. In Section 1.1, we review the emission characteristics of the Sun that are relevant to its use as a calibration source at decimeter wavelengths. In Section 2 we describe the observations and analysis techniques used to produce a beam measurement. Results are presented in Section 3, followed by a discussion of this measurement in the context of the broader CHIME beam measurement program in Section 4.

1.1. Solar Emission at Decimeter Wavelengths

Solar emission at radio wavelengths is conventionally divided into three components: a minimum/quiet component, a slowly varying component, and a burst component. The relative contributions of the latter two fluctuate according to the well-known 11 yr solar cycle. The observations reported here were made in late 2019 and early 2020, near the minimum point between Solar Cycles 24 and 25.[16] The quiet component is produced by thermal free–free (Bremsstrahlung) emission, which, at decimeter wavelengths, originates in the lower corona. Due to steep temperature and density gradients in this part of the solar atmosphere, the brightness temperature of the Sun is a strong function of frequency, with higher frequencies probing lower altitudes and thus lower temperatures.

There is little direct imaging of the Sun in the CHIME band (Shibasaki et al. 2011). However, 432 MHz images from Mercier & Chambe (2012) made during the previous solar minimum (2008–2011) show that emission is nearly uniform over the face of the Sun and is confined to $\lesssim 1.1R_s$, where $R_s = 16'$ is the optical radius of the Sun as viewed from Earth. At higher frequencies, the apparent radius is even closer to the optical radius. We therefore conclude that the emission profile of the Sun throughout the CHIME band can be approximated as a disk with radius $\sim R_s$. Given this radius and the temperature range of the lower corona, the flux density of the quiet Sun is a few $\times 10^5$ Jy in the CHIME band, as shown in Figure 1.

Even at solar minimum, there is still a contribution to the solar flux from slowly varying and burst components. To quantify the amplitude of these components, we refer to total intensity data from the Learmonth Solar Observatory (Australian Bureau of Meteorology 2017), available at 1 s cadence at 410 MHz and 610 MHz. Between 2019 May 31 and 2020 July 11, the standard deviation of the daily mean flux at these frequencies was found to be 7% of the mean value, with a comparable variation on intra-day timescales. Instrumental instability may account for a non-negligible fraction of the variability observed in the Learmonth data, though this contribution is likely small. Nevertheless, we consider this to be an upper limit on the intrinsic solar variability. During this interval, CHIME made calibrated measurements of the solar spectrum four times on days when the Sun was at the decl. of either Tau A or Vir A (2019 May 31, 2019 August 20, 2020 April 21, and 2020 July 11). The beam response at these declinations is independently measured using source fluxes from Perley & Butler (2017), enabling an absolute flux measurement of the Sun on these days. Averaged across the band, these four measurements have a range of 5% relative to the mean. Both the Learmonth and CHIME measurements are plotted in Figure 1. More details about the CHIME flux measurements are described in Section 2.4.

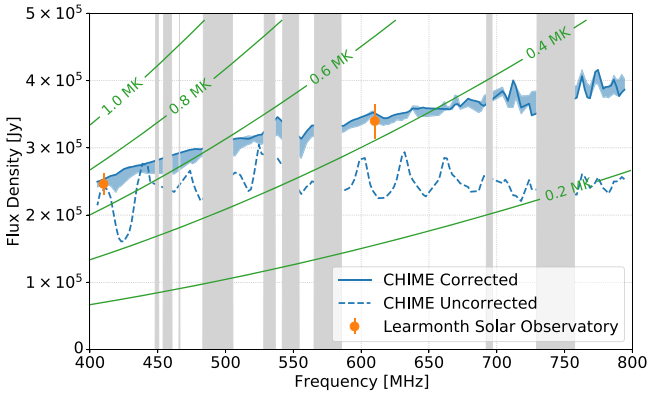

Figure 1. Total solar intensity calibrated against Tau A on 2019 May 31, before (dashed blue) and after (solid blue) correcting for quantization bias (Section 2.5). The shaded blue region covers the range of three other CHIME measurements made at the declinations of Tau A and Vir A through 2020 July 11. Independent measurements of the mean and standard deviation of the daily mean solar flux are shown in orange (Australian Bureau of Meteorology 2017). The gray bars mask frequencies of persistent RFI. The green contours indicate the flux density of a 32′ diameter disk with a given (frequency-independent) brightness temperature, and are shown to emphasize the frequency dependence of the effective temperature of the Sun in this band. Both CHIME and Learmonth observations indicate solar variability <10% over the observation period.

2. Methods

2.1. Data Set

Observations of the Sun are extracted from the CHIME `stack` data set described in detail in CHIME Collaboration et al. (2022a). CHIME is an interferometer that gathers data in the form of correlation products between pairs of feeds. We will therefore discuss the CHIME data in the language of interferometry, where a baseline is the separation between two feeds and a visibility is the correlation product of two voltage streams. By design, the CHIME baseline configuration is highly redundant, enabling data compression by averaging over redundant baselines. Prior to averaging over baselines, data are averaged to 10 s cadence, calibrated for gain variations, and baseline pairs containing bad feeds are masked. Time and frequency bins impacted by radio frequency interference (RFI) are also masked. As these data are recorded as part of CHIME's primary science objectives, no dedicated observing time or specialized data products are needed for this measurement.

[16] National Research Council Canada, https://www.spaceweather.gc.ca/.

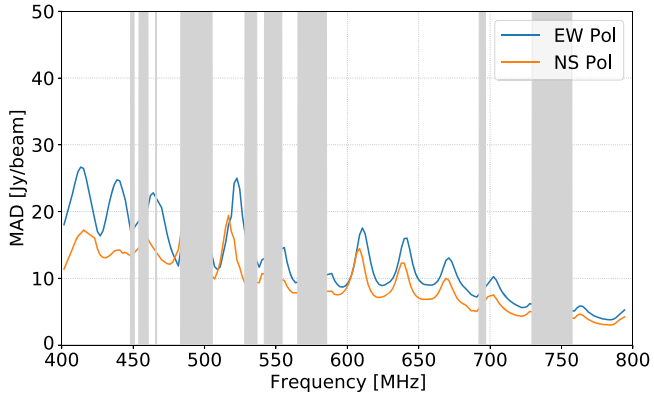

Figure 2. Estimate of confusion noise versus frequency for east–west polarized data (blue) and north–south polarized data (orange). The gray bars mask frequencies of persistent RFI. The difference between the two polarizations is primarily due to the different widths of the primary beams. Confusion noise is estimated as the median absolute deviation (MAD) of the night-time sky brightness over the solar decl. range. On average, the confusion noise is about 4 orders of magnitude lower than the brightness of the Sun (Figure 1). There is a ripple with period 30 MHz due to standing waves between the reflector and the focal line (CHIME Collaboration et al. 2022a).

2.2. Baseline Selection

As described in Section 1.1, the emission profile of the quiet Sun in the CHIME band is well described by a disk approximately 0.5° in diameter. Due to its finite size, only baseline separations between 30 cm and 10 m are used to avoid resolving out the Sun. Zero-spaced baselines (autocorrelations) are masked to remove the receiver temperature bias. Since the minimum east–west separation between feeds is 22 m (set by the spacing of the cylindrical reflectors), this baseline selection only includes purely north–south separations. The corresponding synthesized beam has a north–south width of $\sim 2^\circ$ FWHM at 800 MHz and attenuates the solar flux by $<2\%$ at all frequencies. Finally, only co-polar visibilities are used, with north–south polarized data analyzed separately from the east–west polarized data. After all baseline selection criteria have been applied, 32 unique baselines are used for each polarization.

The selection of baselines also affects the confusion noise limit. Confusion noise is estimated by taking the median absolute deviation (MAD) of the night-time sky brightness over the solar elevation range, using a map made using the same baseline selection as the solar measurements (Figure 2). Full sidereal coverage of the map is achieved by stitching together R.A. ranges observed over the course of the year. Comparing Figures 1 and 2, the flux of the Sun is seen to be about 4 orders of magnitude greater than the confusion noise across most of the band (ignoring beam effects, which are of order unity). Due to the geometry of the reflector, the east–west polarized beam is slightly wider than the north–south polarized beam, resulting in slightly higher confusion noise. The ratio of the solar flux to the confusion noise sets the dynamic range of the beam measurement, which is ~ 40 dB.

2.3. Beamforming

The visibilities from selected baselines (after averaging over redundant baselines) are beamformed to the direction of the Sun. Given the short baselines and large synthesized beam, we treat the Sun as a point source, beamforming only to its center position. The Sun is observed for the full duration that it is above the horizon on each available day between 2019 May 31 and 2020 July 11. Beamformed visibilities are then averaged over the selected baselines, weighted by the inverse noise variance of each visibility. Visibilities in the `stack` data set have been calibrated in units of Jy beam^{-1}, such that this average also has units of Jy beam^{-1}. This interferometric view of the Sun results in a measurement of the average primary beam across the instrument. Variations in the primary beam over individual feeds are not measured, as this would require the full set of redundant visibilities, which are not saved at all frequencies due to data volume considerations.

2.4. Flux Calibration

The flux of the Sun was calibrated once, when the Sun transited at the decl. of Tau A ($+22.7^\circ$) on 2019 May 31. At peak transit (0° hr angle) at this decl., the beam response for each polarization is independently measured using CHIME observations of Tau A and the flux of Tau A reported in Perley & Butler (2017). These beam measurements allow us to calibrate the solar spectrum at this point in time. As discussed in Section 1.1, the average solar flux in the CHIME band varied by $\lesssim 10\%$ between 2019 May 31 and 2020 July 11. Without simultaneous solar monitor data available across the band, we are unable to track the true flux of the Sun to better than this precision and so we treat the flux as constant in this analysis. Among the potential calibrators within the solar decl. range, Tau A is chosen for its high signal-to-noise. Tau A is the brightest radio source in this range and transits at an elevation where the CHIME primary beam response is also high. As a cross-check, the flux of the Sun was calibrated again against Tau A on 2020 July 11, and against Virgo A on 2019 August 20 and 2020 April 21. As shown in Figure 1, these measurements agree to within 5% across the band.

2.5. Correcting for Quantization Bias

The dynamic range of the CHIME correlator is limited by the bit depth of the channelized voltages, which are rounded to four real bits and four imaginary bits prior to correlation (Bandura et al. 2016). While this bit depth is sufficient for CHIME's primary science objectives, it introduces a bias due to digital compression when the Sun is in the main lobe of the primary beam. If left uncorrected, this effect can bias the solar spectrum by as much as $\sim 30\%$ in amplitude, as shown in Figure 1. We account for this effect using an approximation of the analytical corrections derived in Benkevitch et al. (2016) and Mena-Parra et al. (2018) for complex digital correlators. For a complete description, the reader should refer to these publications, though we will briefly describe the process here.

Equation (21) of Benkevitch et al. (2016) provides an analytical expression for the quantized correlation $\hat{\kappa}_{ij}$ given the true, unquantized correlation, κ_{ij}, as well as the standard deviations of inputs i and j. We will refer to this function as g.

$$\hat{\kappa}_{ij} = g(\kappa_{ij}, \sigma_i, \sigma_j) \tag{1}$$

Similarly, Equation (8) of Mena-Parra et al. (2018) provides an expression for the quantized standard deviation as a function, f, of the true standard deviation.

$$\hat{\sigma} = f(\sigma) \tag{2}$$

The objective is to recover the true correlation, κ, when only the quantized quantities, $\hat{\sigma}$ and $\hat{\kappa}$, are known. This is

accomplished by inverting Equations (1) and (2) as follows:

$$\begin{aligned}\kappa_{ij} &= g^{-1}(\hat{\kappa}_{ij}, \sigma_i, \sigma_j) \\ &= g^{-1}(\hat{\kappa}_{ij}, f^{-1}(\hat{\sigma}_i), f^{-1}(\hat{\sigma}_j))\end{aligned}. \quad (3)$$

Our analysis makes two further simplifying assumptions. The first assumption is to ignore the phase error of $\hat{\kappa}$ and only to correct for amplitude. At peak signal level, the phase error in a single baseline due to compression is $\sim 10'$ and becomes negligible ($\lesssim 10''$) when averaged over redundant baselines. Second, because the CHIME `stack` data set has been averaged over redundant baselines, we need to assume that $\hat{\sigma}_i^2 = \hat{\sigma}_j^2 = \langle \hat{\sigma}^2 \rangle$ and $\hat{\kappa}_{ij} = \langle \hat{\kappa} \rangle$ for all inputs i, j in each unique baseline. However, since the CHIME offline data set does include the full correlation matrix (which has not been averaged over redundant baselines) at four frequencies, we can compare the exact analytical correction to our simplified version at these frequencies. We find that the error incurred by averaging over redundant baselines is $\lesssim 1\%$, less than the intrinsic flux variation of the Sun.

3. Results

The power beam ratio is formed by dividing the measured response to the Sun in each direction by the calibrated flux of the Sun. We normalize the beam to unity at the transit of Cyg A (0° hr angle, +40.7° decl.) to be consistent with how the data are normalized by the complex gain calibration procedure (for details, see CHIME Collaboration et al. 2022a). As a consequence, the beam will have values greater than one in some directions.

Each solar transit traces a line of approximately constant decl. The transit on 2019 August 20, when the Sun was at the decl. of Vir A (+12.4°), is shown in Figure 3. Throughout the year, the daily change in solar decl. is less than the ∼0.5° diameter of the Sun, enabling consecutive transits to be stitched together to achieve continuous decl. coverage. The full solar decl. range was observed twice: first in late 2019 and again in early 2020. Due to planned software deployments and telescope maintenance resulting in instrument downtime, certain decl. ranges were missed in 2019. In 2020, deployments were planned to avoid missing the same decl. ranges twice, enabling complete decl. coverage in the combined data set.

The combined data set at 600 MHz is shown in Figure 4 using an orthographic projection with its origin at the zenith. This projection has the advantage of not distorting the apparent beamwidth at different elevations and the projected coordinates x and y are always parallel to east and north, respectively. The coordinates x and y are the projections of the unit vector pointing to hour angle h and decl. δ, given by

$$x = -\cos\delta \sin h \quad (4)$$

and

$$y = \cos\delta_0 \sin\delta - \sin\delta_0 \cos\delta \cos h \quad (5)$$

where δ_0 is the latitude of the observer (+49.3° for CHIME). The basic shape of the beam in Figure 4 can be described as a 1°–4° wide stripe along the local meridian, with moderate (−20 dB) side lobes extending up to 20° on either side. As shown in Figure 5, the amplitude and width of the main lobe vary considerably (∼25%) over modest changes in frequency and elevation angle. There is also significant structure in the side lobes of both polarizations. Though difficult to quantitatively predict, these variations are qualitatively expected due to multiple reflection paths within the telescope, cross talk between feeds, and blockages in the aperture. For a more in-depth discussion of these beam features, we refer the reader to CHIME Collaboration et al. (2022a).

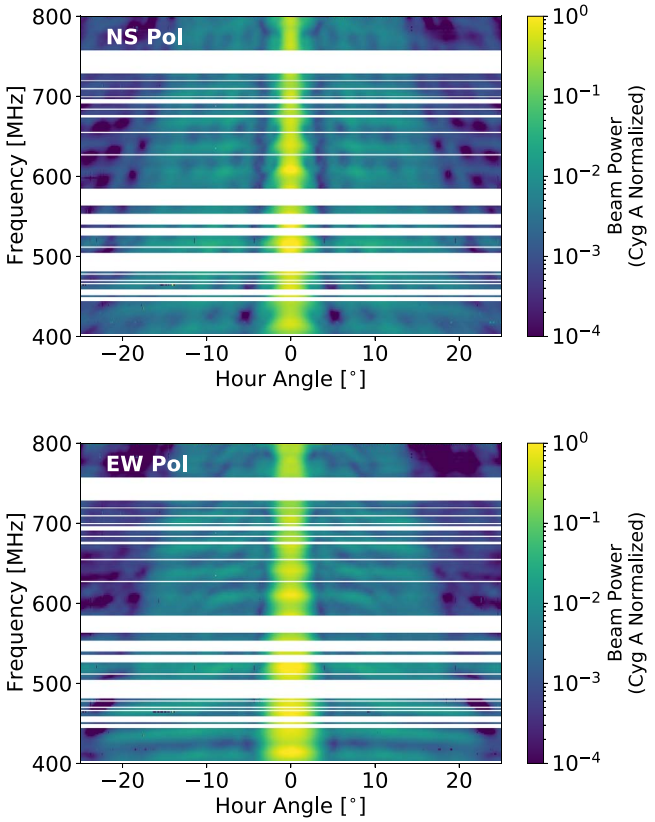

Figure 3. North–south (top) and east–west (bottom) polarized beam measurements from a single solar transit on 2019 August 20, when the Sun was at the decl. of Vir A (+12.4°). On large frequency scales, the beamwidth is proportional to wavelength, as expected due to diffraction. There is also a modulation in the beam amplitude and width on 30 MHz scales, due to standing waves between the reflector and the focal line. By convention in CHIME, the beam is normalized to be 1 at the transit of Cyg A (0° hour angle, +40.7° decl.)

Where repeat observations are available, the two measurements are averaged and their difference is used to assess measurement repeatability (Figure 6). In regions where the response to the Sun is much greater than the confusion noise, we expect the difference between measurements to be dominated by variations in the flux of the Sun. Comparing Figures 4 and 6, where the beam response is greater than 10^{-3} ($\gtrsim 10\times$ the confusion limit), the fractional difference is found to be 9% at 600 MHz, which is comparable with our estimate of solar variability over the observation period. Where the beam response is less than 10^{-3}, the measurement becomes increasingly confusion-noise limited, causing the fractional error to increase.

3.1. Comparison with Other Beam Measurements

The solar beam measurements are only part of the broader CHIME beam measurement program. Although the Sun probes about 7200 square degrees, additional measurements are needed to span the full sky. Where spatial overlap exists between measurements, we can make comparisons. The other

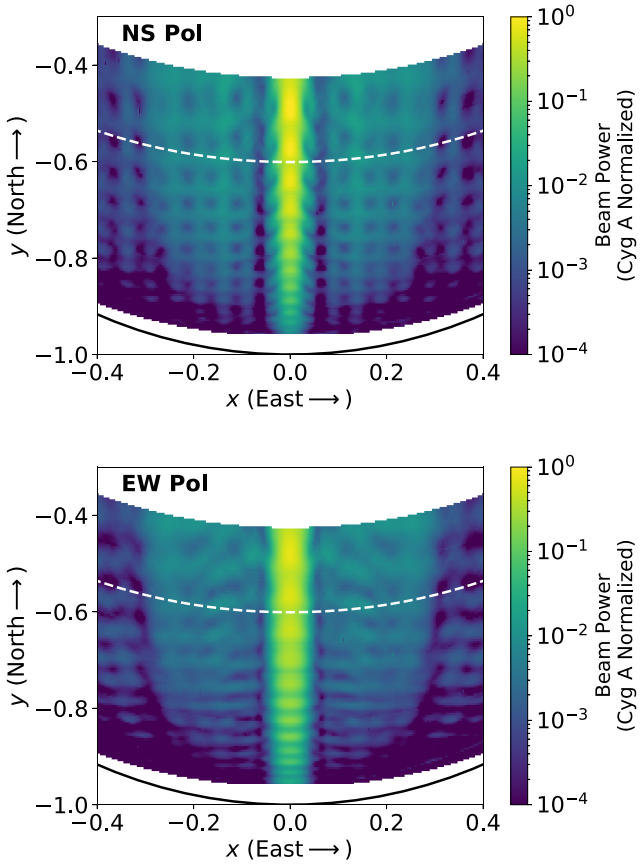

Figure 4. Orthographic projection of the north–south (top) and east–west (bottom) polarized beam measurements at 600 MHz, made by combining one year of solar transits. The modulation in beamwidth on small angular scales is real and arises from multiple reflection paths within the telescope. The white dashed line marks the path of the Sun made during the transit shown in Figure 3. The black curved line near the bottom of the plot marks the southern horizon. The zenith (off-scale) is located at the coordinate (0,0).

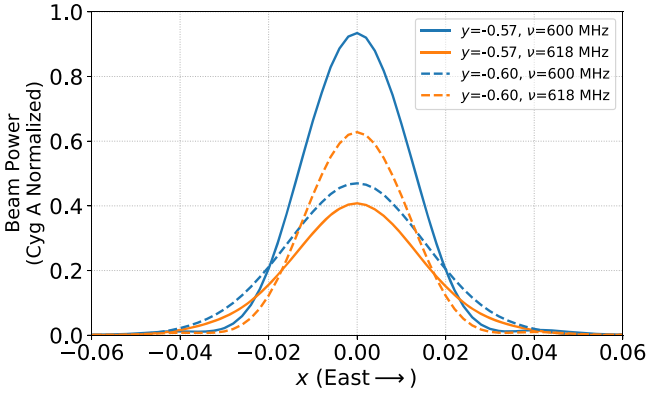

Figure 5. Slices of the north–south polarized beam as a function of orthographic coordinate x, emphasizing the evolution of the beam profile over frequency and elevation angle. Beam slices at 600 MHz (618 MHz) are plotted in blue (orange). Beam slices at $y = -0.57$ (-0.60) are plotted with solid (dashed) lines. The variations in beam amplitude and width arise due to interference between multiple reflection paths within the telescope. Rays with multiple reflections have broader illumination compared to the primary ray, resulting in narrower beamwidths at frequencies and angles corresponding to constructive interference (solid blue and dashed orange lines).

measurements all rely on astrophysical point-source observations and thus have complementary systematics to the solar measurement. In general, the fluxes of these sources are more

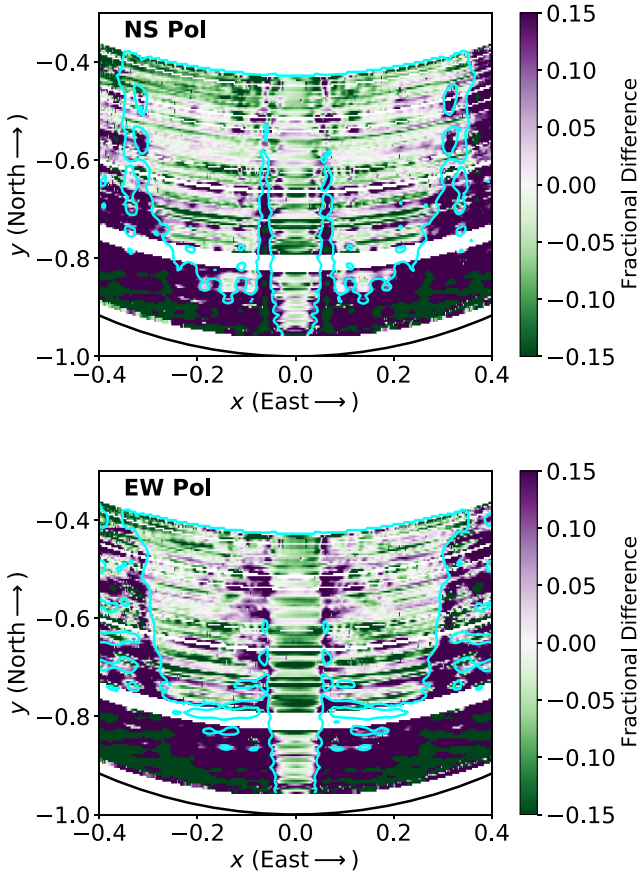

Figure 6. The fractional difference between measurements made in late 2019 and early 2020, shown for the north–south (top) and east–west (bottom) polarized beam at 600 MHz. White space corresponds to where only a single measurement exists. Where the beam response in Figure 4 is greater than 10^{-3} (cyan contour), the measurement uncertainty is dominated by intrinsic solar variability. Below this level, confusion noise is comparable to or larger than the effect of solar variability. For both polarizations, the fractional differences within the contour approximately follow a normal distribution with $\sigma = 9\%$.

stable than the Sun (though they may have large uncertainties) and are small enough to not require correction for quantization bias. Additionally, point-source observations can be made with a complementary set of baselines, since these sources are unresolved by CHIME's longest baselines.

The angular coverage of the different beam measurements is summarized in Figure 7. There are two categories of measurements that rely on astrophysical point sources: source tracks and deconvolutions. The former is made by beamforming visibilities to the location of bright sources as they transit through the primary beam, analogously to how the solar measurement is made. Beamforming may be done with CHIME-only baselines, or with baselines between CHIME and the John A. Galt 26 m tracking telescope (Locke et al. 1965) using the holographic technique described in Berger et al. (2016). Holographic measurements have the added benefit of measuring the beam phase in addition to amplitude. The second type of point-source beam measurement is made by deconvolving a model of the point-source sky from a CHIME map as described in CHIME Collaboration et al. (2022b). Unlike the source tracks, which probe discrete declinations over a moderately wide range in hour angle, the deconvolved beam has continuous decl. coverage, but is limited to the width of the main lobe in the east–west direction.

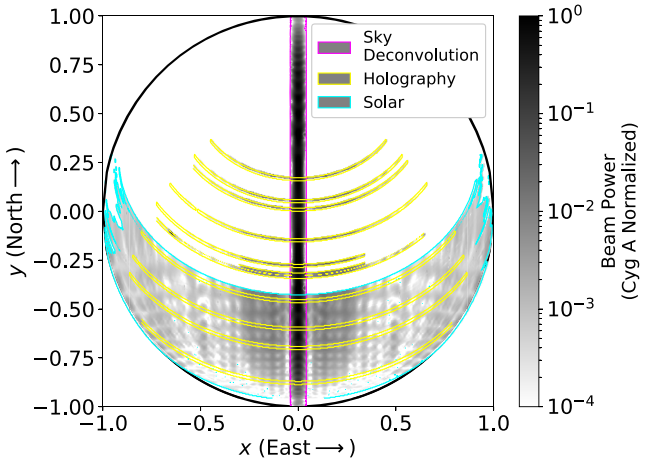

Figure 7. Orthographic projection of multiple north–south polarized beam measurements at 600 MHz. Despite spanning more than 7200 square degrees, the solar measurement (cyan outline) only probes the main lobe between $y = -0.44$ and $y = -0.95$. In contrast, the beam measurement derived by deconvolving a point-source model of the sky (magenta outline) spans the full elevation range of the main lobe, but does not probe the side lobes. Holography tracks of the brightest point sources (yellow outline) probe the beam at discrete elevations over a wide range in hour angle. The black circle marks the horizon.

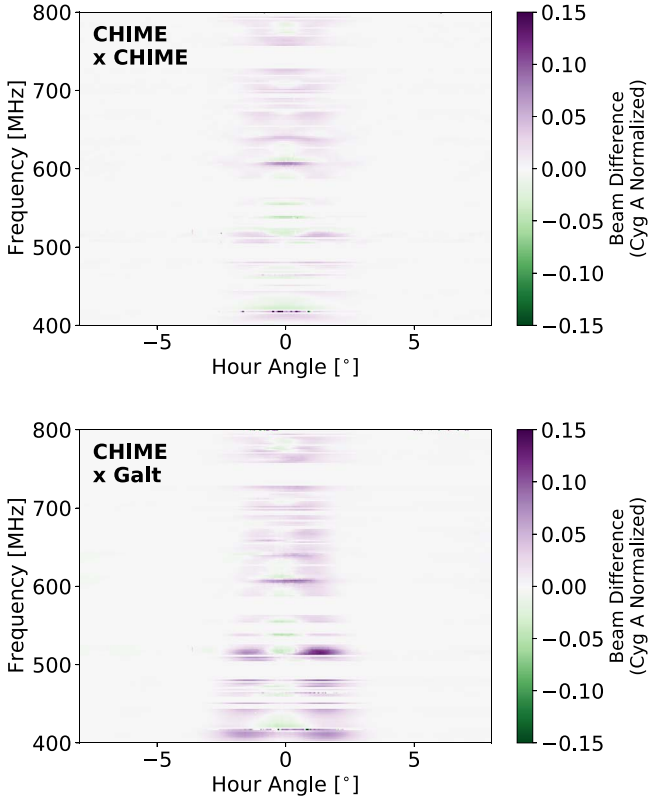

Figure 8. The difference between the solar measurement of the north–south polarized beam at the decl. of Vir A (+12.4°) and a CHIME-only measurement of Vir A (top), and a holographic measurement of Vir A (bottom). Systematic differences between beam measurements are typically less than a few percent of the peak beam response, and are primarily due to percent-level differences in measured beamwidth. Systematic differences between the east–west polarized beam measurements (not shown) are approximately a factor of two larger.

In Figure 8, we show the difference between the solar measurement at the decl. of Vir A (+12.4°) and source tracks of Vir A. Note that, unlike Tau A, Vir A was not explicitly used to calibrate the flux of the Sun and thus provides a truly independent measurement of the beam. While the CHIME-only observation of Vir A provides slightly better agreement with the solar measurement than does the holographic measurement, both comparisons reveal systematic differences which are small —typically a few percent of the peak beam response. Residuals are dominated by systematic differences in the east–west width of the main lobe. For the north–south polarized beams shown in Figure 8, the solar beam is on average 2% wider than the CHIME-only measurement of Vir A, and 6% wider than the holographic measurement.

In Figure 9 we plot the north–south polarized beam at $x = 0$ as a function of y and frequency, as well as the difference between this beam and the deconvolved point-source beam. Currently, the deconvolved point-source beam has only been evaluated at frequencies greater than 585 MHz. Again, the level of agreement is typically a few percent of the peak response, though there are some large excursions around 600 MHz. We also find that the solar beam measurement is systematically wider than the deconvolved point-source beam by ∼5% in both polarizations. These differences in width are larger than can be explained by the angular extent of the Sun and efforts to understand the discrepancies between measurements are ongoing.

4. Discussion

In this section we will discuss the utility of this beam measurement in the context of CHIME science. As its name suggests, one of CHIME's primary science objectives is to map the distribution of neutral hydrogen in the low-redshift ($z \sim 1$) universe. It is difficult to generalize the beam knowledge requirements to meet this objective, since any statement on beam accuracy depends on both the details of the analysis and the form of the beam errors. To give one example, the analysis presented in Shaw et al. (2015) using m-mode formalism and a Karhunen–Love (KL) transform for foreground removal concluded that the beamwidth had to be known to an accuracy of 10^{-3} in order to avoid foreground contamination of the 21 cm power spectrum. For comparison, we found in Section 3.1 that the east–west width of the solar beam measurements were discrepant with other measurements at the level of a few percent, or about one and a half orders of magnitude worse than the desired accuracy for this particular analysis.

However, there are reasons for optimism. First, the modeled beamwidth errors in Shaw et al. (2015) were drawn from a random distribution, resulting in power leakage from low-k, foreground-dominated modes to higher k signal modes. In contrast, the errors in this measurement are highly correlated in frequency, affecting the high-k modes to a lesser degree. Second, the use of alternative foreground removal techniques, instead of or in conjunction with the KL transform, may relax requirements on instrumental knowledge. The degree to which both of these factors impact the ultimate analysis is a subject of an ongoing investigation.

Nevertheless, these solar beam measurements bring us significantly closer to achieving CHIME's cosmology goals and, in combination with other beam measurements, have enabled the first 21 cm detection with CHIME (CHIME Collaboration et al. 2022b). These measurements can also be used to aid in interpolating between the comparatively sparse point-source beam measurements that are outside the solar decl. range, bringing us closer to a full 2π description of the beam.

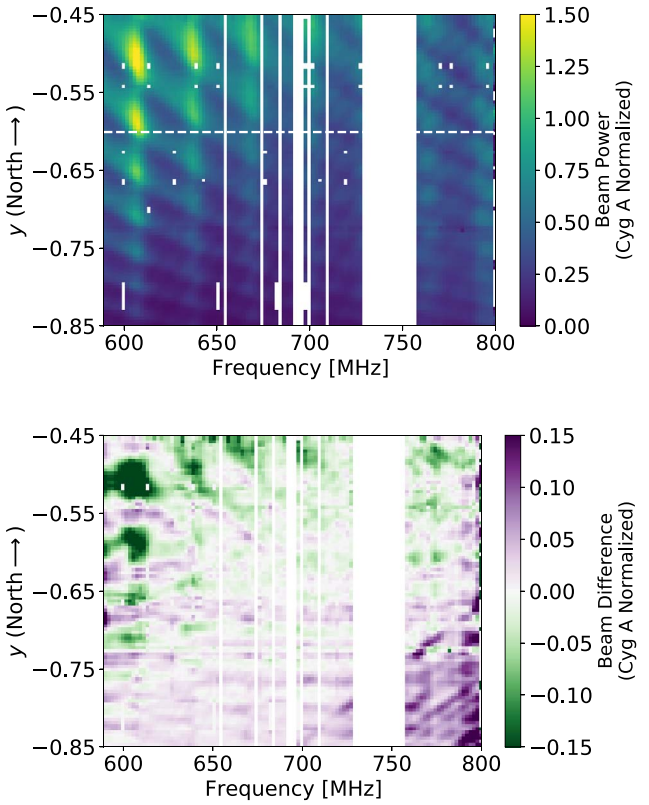

Figure 9. The solar measurement of the north–south polarized beam as a function of orthographic coordinate y and frequency (top), and the difference compared to the corresponding measurement made by deconvolving a point-source model of the sky from a long-baseline CHIME map (bottom). The white dashed line in the top panel marks the position of the Sun during the transit shown in Figure 3. For both the north–south and east–west polarized beams (latter not shown), the differences are approximately normally distributed with $\sigma = 0.04$ in Cyg A normalized units.

As shown in Figure 7, the solar measurement is the only data set to provide significant information about the 2D spatial structure of the primary beam. While the structure appears rather complicated, in fact it is highly separable in x and y and its variance is dominated by a few separable spatial modes at each frequency. This relative simplicity is being used to guide us in how to interpolate between point-source measurements over the rest of the sky. One approach we are currently exploring is to derive a set of basis functions in x from the solar data, which are then fit to the point-source data near the meridian, at each y and frequency. These efforts show promising early results.

In addition to such data-driven analyses, the solar data can also be used to improve our physical understanding of the telescope. As mentioned in Section 3, the complicated spatial structure of the beam is qualitatively expected due to multipath and receiver cross-talk effects within the telescope. We have been developing a coupling model similar to that described by Kern et al. (2019) that may be fit to our full set of beam measurements. The solar data play a key role in constraining the off-meridian properties of this model, which account for 10%–20% of CHIME's total primary beam solid angle.

These solar beam measurements are also applicable to CHIME observations of fast radio bursts and pulsars, which have considerably less stringent requirements on beam uncertainty compared to the cosmological measurement. The beam models used in CHIME/FRB Collaboration et al. (2021) and Good et al. (2021) were each informed in part by these data. Also, in combination with a holographic measurement of Tau A, these data were used to calibrate the spectral flux density of the flare observed from Galactic magnetar SGR 1935 +2154 reported in CHIME/FRB Collaboration et al. (2020).

5. Conclusions

We have presented a measurement of the CHIME primary beam pattern using the Sun as a calibration source. This data set is an integral part of the broader CHIME beam measurement program, complementing more conventional beam measurements using astrophysical point sources. This data set provides a direct measurement of the CHIME beam at low decl. and is indeed the only measurement over much of the sky. Where overlap exists with other beam measurements, comparisons can be made to constrain the systematics of different measurement techniques. The rich spatial structure revealed by this measurement has enormous qualitative and quantitative value for understanding the source of beam features and may enable extrapolating beyond the current measurement. Efforts to combine beam measurements will be the topic of future publications.

The semiannual motion of the Sun enables measuring a large solid angle without the need to move the telescope, which is particularly useful for drift-scan instruments. Despite the intrinsic variability of the Sun, the uncertainty on the resulting beam measurement is estimated to be $<10\%$ where the response is above the confusion limit, which is $\sim$40 dB below the peak beam response. While CHIME was able to take advantage of the solar minimum period for these observations, future instruments wishing to use the Sun for beam measurements may find themselves poorly situated with respect to the 11 yr solar cycle. However, solar beam measurements may still be viable in times of increased solar activity. Whereas this analysis made no attempt to correct for variations in the solar flux, even simple adjustments based on independently available solar monitor data may be sufficient to account for the slowly varying component of solar emission.

We thank the Dominion Radio Astrophysical Observatory, operated by the National Research Council Canada, for leasing the CHIME site and for their gracious hospitality and support. DRAO is situated on the traditional, ancestral, and unceded territory of the Syilx Okanagan people. We are fortunate to live and work on these lands. CHIME is funded by grants from the Canada Foundation for Innovation (CFI) 2012 Leading Edge Fund (Project 31170), the CFI 2015 Innovation Fund (Project 33213), and by contributions from the provinces of British Columbia, Québec, and Ontario. Long-term data storage and computational support for analysis are provided by WestGrid[17] and Compute Canada.[18]

Additional support was provided by the University of British Columbia, McGill University, and the University of Toronto. CHIME also benefits from NSERC Discovery Grants to several researchers, funding from the Canadian Institute for Advanced Research (CIFAR), and from the Dunlap Institute for Astronomy and Astrophysics at the University of Toronto, which is funded through an endowment established by the David Dunlap family. This material is partly based on work

[17] https://www.westgrid.ca
[18] https://www.computecanada.ca

supported by the NSF through grants No. 2008031, 2006911, and 2006548, and by the Perimeter Institute for Theoretical Physics, which in turn is supported by the Government of Canada through Industry Canada and by the Province of Ontario through the Ministry of Research and Innovation.

Facilities: CHIME (CHIME Collaboration et al. 2022a), Learmonth Solar Observatory (Australian Bureau of Meteorology 2017), John A. Galt Telescope (Locke et al. 1965).

Software: NumPy (Harris et al. 2020), SciPy (Virtanen et al. 2020), HDF5 (The HDF Group 1997), h5py (Collette et al. 2021), Matplotlib (Hunter 2007), Skyfield (Rhodes 2019), caput (Shaw et al. 2020a), ch_pipeline (Shaw et al. 2020b), draco (Shaw et al. 2020c), kotekan (Renard et al. 2021).

ORCID iDs

Mandana Amiri https://orcid.org/0000-0001-6523-9029
Kevin Bandura https://orcid.org/0000-0003-3772-2798
Jean-François Cliche https://orcid.org/0000-0001-6509-8430
Meiling Deng https://orcid.org/0000-0001-8123-7322
Matt Dobbs https://orcid.org/0000-0001-7166-6422
Mateus Fandino https://orcid.org/0000-0002-6899-1176
Simon Foreman https://orcid.org/0000-0002-0190-2271
Mark Halpern https://orcid.org/0000-0002-1760-0868
Alex S. Hill https://orcid.org/0000-0001-7301-5666
Gary Hinshaw https://orcid.org/0000-0002-4241-8320
Carolin Höfer https://orcid.org/0000-0003-4887-8114
Joseph Kania https://orcid.org/0000-0002-3354-3859
T. L. Landecker https://orcid.org/0000-0003-1455-2546
Joshua MacEachern https://orcid.org/0000-0001-8064-6116
Kiyoshi Masui https://orcid.org/0000-0002-4279-6946
Juan Mena-Parra https://orcid.org/0000-0002-0772-9326
Laura Newburgh https://orcid.org/0000-0002-7333-5552
Anna Ordog https://orcid.org/0000-0002-2465-8937
Tristan Pinsonneault-Marotte https://orcid.org/0000-0002-9516-3245
Ava Polzin https://orcid.org/0000-0002-5283-933X
Alex Reda https://orcid.org/0000-0001-6967-7253
J. Richard Shaw https://orcid.org/0000-0002-4543-4588
Seth R. Siegel https://orcid.org/0000-0003-2631-6217
Saurabh Singh https://orcid.org/0000-0001-7755-902X
Keith Vanderlinde https://orcid.org/0000-0003-4535-9378
Haochen Wang https://orcid.org/0000-0002-1491-3738
Dallas Wulf https://orcid.org/0000-0001-7314-9496

References

Australian Bureau of Meteorology 2017, SWS Solar Radio Data from Learmonth (1991 Onwards), http://www.bom.gov.au/metadata/19115/ANZCW0503900486
Bailes, M., Jameson, A., Flynn, C., et al. 2017, PASA, 34, e045
Bandura, K., Bender, A. N., Cliche, J. F., et al. 2016, JAI, 05, 1641005
Benkevitch, L. V., Rogers, A. E. E., Lonsdale, C. J., et al. 2016, arXiv:1608.04367
Berger, P., Newburgh, L. B., Amiri, M., et al. 2016, Proc. SPIE, 9906, 99060D
Chang, C., Monstein, C., Refregier, A., et al. 2015, PASP, 127, 1131
CHIME Collaboration, Amiri, M., Bandura, K., et al. 2022a, arXiv:2201.07869
CHIME Collaboration, Amiri, M., Bandura, K., et al. 2022b, arXiv:2202.01242
CHIME/FRB Collaboration, Amiri, M., Andersen, B. C., et al. 2021, ApJS, 257, 59
CHIME/FRB Collaboration, Andersen, B., Bandura, K., et al. 2020, Natur, 587, 54
Collette, A., Kluyver, T., Caswell, T. A., et al. 2021, h5py/h5py: v3.5.0, Zenodo, doi:10.5281/zenodo.5585380
Crichton, D., Aich, M., Amara, A., et al. 2022, JATIS, 8, 011019
Good, D. C., Andersen, B. C., Chawla, P., et al. 2021, ApJ, 922, 43
Harris, C. R., Millman, K. J., van der Walt, S. J., et al. 2020, Natur, 585, 357
Higgs, L. A., & Tapping, K. F. 2000, AJ, 120, 2471
Hunter, J. D. 2007, CSE, 9, 90
Kern, N. S., Parsons, A. R., Dillon, J. S., et al. 2019, ApJ, 884, 105
Kocz, J., Ravi, V., Catha, M., et al. 2019, MNRAS, 489, 919
Locke, J. L., Galt, J. A., & Costain, C. H. 1965, PDO, 25, 77
Mena-Parra, J., Bandura, K., Dobbs, M. A., Shaw, J. R., & Siegel, S. 2018, JAI, 07, 1850008
Mercier, C., & Chambe, G. 2012, A&A, 540, A18
Murphy, E. M. 1993, PhD thesis, Charlottesville, VA
Pauliny-Toth, I. K., & Shakeshaft, J. R. 1962, MNRAS, 124, 61
Perley, R. A., & Butler, B. J. 2017, ApJS, 230, 7
Phan, A. & Tianlai Collaboration 2020, BAAS, 52, 3
Renard, A., Shaw, R., Ng, C., et al. 2021, Kotekan: A Framework for High-performance Radiometric Data Pipelines, 2021.11, Zenodo, doi:10.5281/zenodo.5842660
Rhodes, B. 2019, Skyfield: High Precision Research-grade Positions for Planets and Earth Satellites Generator, Astrophysics Source Code Library, ascl:1907.024
Shaw, J. R., Masui, K., Hincks, A. D., et al. 2020b, chime-experiment/ch_pipeline: v20.10.0, Zenodo, doi:10.5281/zenodo.5846379
Shaw, J. R., Masui, K., Nitsche, R., et al. 2020a, radiocosmology/caput: v20.10.0, Zenodo, doi:10.5281/zenodo.5846375
Shaw, J. R., Sigurdson, K., Sitwell, M., Stebbins, A., & Pen, U.-L. 2015, PhRvD, 91, 083514
Shaw, R., Nitsche, R., Siegel, S. R., et al. 2020c, radiocosmology/draco: v20.10.0, Zenodo, doi:10.5281/zenodo.5828373
Shibasaki, K., Alissandrakis, C. E., & Pohjolainen, S. 2011, SoPh, 273, 309
The HDF Group 1997, Hierarchical Data Format, version, 5 https://www.hdfgroup.org/HDF5/
Vanderlinde, K., Liu, A., Gaensler, B., et al. 2019, The Canadian Hydrogen Observatory and Radio-transient Detector (CHORD), Tech. rep, 28
Virtanen, P., Gommers, R., Oliphant, T. E., et al. 2020, NatMe, 17, 261
Zhang, J., Liu, J., Wu, F., et al. 2021, IAPM, 63 (6) 98